Heliyon 9 (2023) e19655

Contents lists available at ScienceDirect

Heliyon

journal homepage: www.cell.com/heliyon

Hybrid system model for wind abrasion segmentation using semi-automatic classification of remote sensing multispectral areas

Marta Terrados-Cristos *, Francisco Ortega-Fernández, Marina Díaz-Piloñeta, Vicente Rodríguez Montequín, José Valeriano Álvarez Cabal

Project Engineering Department, University of Oviedo, 33004, Oviedo, Spain

ARTICLE INFO

Keywords:
Remote sensing
Wind erosion
GIS
Abrasion
Metallic resilient structures

ABSTRACT

Wind abrasion, caused by particles transported by strong winds impacting on structures, can lead to their degradation. Although this phenomenon has hardly been studied in this context, it is becoming increasingly important due to new trends in infrastructure location, especially in renewable energy terms. Metallic structures are particularly vulnerable to degradation by the action of windblown sand particles. However, characterising such secluded sites is complicated, and remote sensing systems and satellite information become crucial. The objective of this research is to identify and delineate the geographic areas that are vulnerable to this phenomenon by employing a hybrid model with historical data and the semi-automatic classification of multispectral satellite images. The model is based on critical variables identified by the scientific community and case studies documented in the literature. The methodology used for the study consists of four phases, including creating a scientifically robust database, downloading and managing satellite and historical long-term information, segmenting the regions of interest, and modelling using supervised classification techniques. The proposed algorithm shows very accurate results ($R^2 = 0.9922$) and the overall system approach is presented as a useful and generalizable method to address this problem, increasing the existing knowledge on material wear by particle action, and contributing to optimizing the initial design of resilient structures.

1. Introduction

Structural degradation is not only associated with structural problems, but also with economic, environmental and social problems [1]. Managing degradation and creating resilient structures is a major issue and a constant challenge [2]. There are different mechanisms of material degradation, the principal ones being: corrosion [3] and abrasion [4]. Corrosion is the process of decomposition of a material caused by a chemical reaction with its environment [5], while abrasion is a physical erosion process produced by particles impacting solid objects [6].

In dry regions, and areas with insufficient rainfall to support vegetation, there is a greater likelihood of degradation of adjacent structures. Erosion is a complex phenomenon that can occur in very different environments. However, there are some basic characteristics that locations susceptible to this phenomenon must share. Situations of low relative humidity, high wind speeds and high

* Corresponding author.
E-mail address: marta.terrados@api.uniovi.es (M. Terrados-Cristos).

https://doi.org/10.1016/j.heliyon.2023.e19655
Received 10 May 2023; Received in revised form 29 August 2023; Accepted 29 August 2023
Available online 3 September 2023

amounts of airborne particles are likely to carry sand by the wind and impact on surrounding constructions [6]. The mechanism of wind-blown sand transport that mainly influences this phenomenon is saltation, and it is related to the movement of particles with diameters between 0.07 and 0.50 mm [7]. Furthermore, soil composition and clay content in the soil makes it more aggressive towards the metal, which influences the efficiency of water absorption [8].

Particle erosion has been studied in various contexts. There are models for soil erosion [9–12], computational models for pipeline erosion control, especially in the oil and gas industry [13–18], modelling with CFD (computational fluid dynamics), finite element models [19], ANSYS or ABAQUS software [13,20] and new methods based on 'bipolar electrochemistry' [21]. Unfortunately, all these findings are not directly applicable to abrasion caused by wind-driven particles, since liquid transport fluids have greater carrying capacity, thus transporting more and much larger particles.

Moreover, this phenomenon not only affects infrastructure stability in general but different sectors, in particular. For example, it also impacts the reflectance loss of solar panels [22], increasing the weight to be supported by the structures, the burying of infrastructures and, even, corrosion [23]. In some cases, this phenomenon can be diminished by physical mitigation systems [24,25], although the most common way is to improve material protection [26,27] with a consequent rise in cost. However, such cases are challenging and are having an increasing impact. For example, on the north-west coast of Egypt, sandstorms wear down buildings [28].

Nevertheless, the action of windblown sand and its effects on civil structures and infrastructure are almost entirely overlooked in the literature [25], which makes it difficult to unify the work and complicates the monitoring of these issues. The reason for the little attention being paid to this problem may lie in the fact that most locations are not a priori susceptible to these circumstances [7]. The regions which are potentially susceptible to the action of windblown sands are coastal dunes [29], active sand deposits [30] and degraded lands [22], occupying about one-fifteenth of the Earth's surface [31]. However, such areas increasingly host human activities, such as transport, industrial, mineral exploitation, residential uses and renewable energies. More and more civil structures and infrastructure are being built in desert and coastal regions [32,33]. In addition, climate change has a strong impact on environmental conditions [34] and sandstorms occur much more frequently [35]. Accordingly, since this is a physical phenomenon with a cumulative impact, the number of risky events will also increase. Therefore, there is a need to update environmental measures, to properly design new structures and ensure the reliability of existing ones.

In this context, using geographic information system (GIS) techniques for processing and analysing data containing spatial information [36] derived from remote sensing [37], it is proposed to characterise and locate areas susceptible to such problems. Many studies use these technologies to classify and diagnose the health of the earth's crust, soils and vegetation [38–41]. Specifically, the use of remote sensing and GIS techniques is beginning to be used in this context, to assess sand dune hazards [42], but there are no studies that globally characterise the susceptibility and risk potential of a given area. Moreover, the specific problem of degradation of metallic structures by abrasion is more complex, as it requires not only the study of the ground cover but also the influence of other critical factors, such as granulometry, composition and climatic characteristics. This makes it necessary to gather extensive long-term data, in order to understand the underlying mechanisms and develop effective solutions.

Knowing and classifying the earth's surface is interesting, with respect to constructive engineering and structural design. Examples of mitigation measures [43–46] or equations for modelling the impact of this degradation [13,47] are currently available; however, there are currently no existing tools that allow us to predict potential risks beforehand or create suitable designs, based on a hybrid model comprising historical data and multispectral imagery, to identify problematic areas.

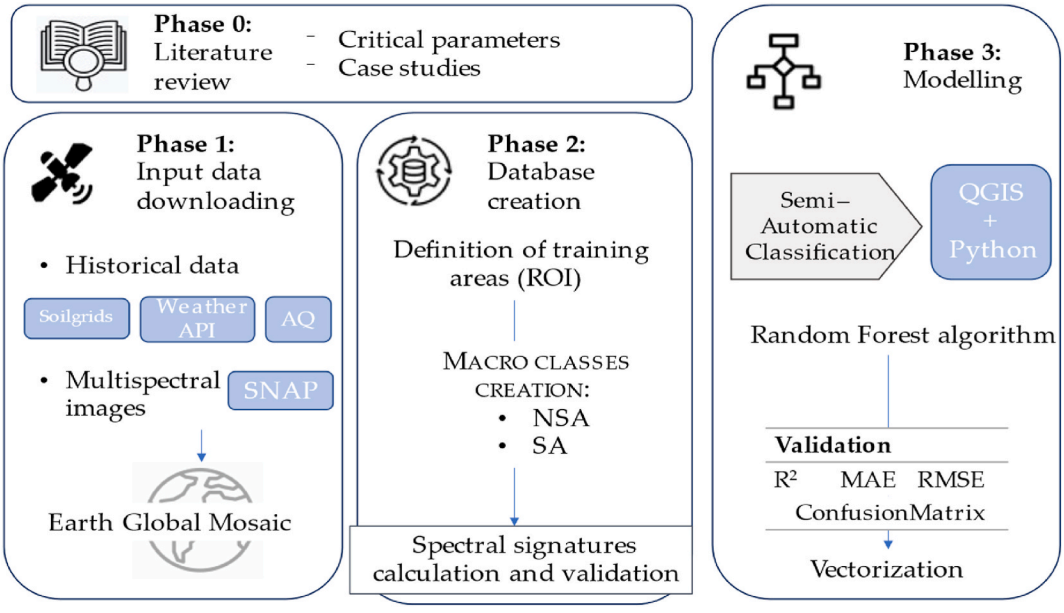

Fig. 1. Overall process followed.

The primary objective of this study is to develop a comprehensive world map that identifies areas prone to wind abrasion. The aim is to leverage potential remote sensing and multispectral image analysis technologies to classify global terrains based on historical data and case studies. The ultimate goal is to characterise diverse environments without the need for costly on-site sampling and location assessments, providing generalized results applicable anywhere in the world. By achieving this, the study aims to significantly address the issue of wind erosion and associated problems related to sand transport in eroded soils. Ultimately, this research aims to reduce uncertainty in the initial stages of construction projects in these vulnerable areas, ensuring a more informed understanding of theirdimensional requirements. This paper begins by providing a comprehensive explanation of the methodology used. The approach encompasses the identification of case studies, actual historical data, and training variables to train the model. Subsequently, the creation of the database is discussed, which involves characterising each region of interest through multispectral images. The paper then outlines the modelling and evaluation techniques employed in the study. Lastly, the results are examined and the conclusions derived from this research are presented.

2. Materials and methods

Developing a model for wind abrasion segmentation requires a robust database with validated information from various sources. This data serves as a basis for applying regression and classification models, which enable the identification of problematic areas and the drawing of conclusions about the impact of the wear problem on their metal structures. The resulting model is a hybrid system model, integrating the strengths of combining different data types and processing techniques. The method used is summarised in Fig. 1 and involved four main phases. The preliminary phase included a thorough literature review to find case studies and real scenarios to base the model training on. Finding suitable case studies is crucial for developing effective solutions but gathering accurate and relevant data can pose significant challenges. The first phase consisted of multi-spectral image processing and historical information downloading for the specified study locations. During the second phase, the training areas were created based on the analysed data and, finally, the third phase consisted of global modelling. The freeware tools used in each case are shown in blue.

2.1. Phase 0: literature review

The most reliable option for assessing the real danger of erosion caused by sandstorms was through real-life exposure to certain materials. However, this can be a time-consuming task.

Since the problem studied here was scarcely addressed in the literature, a careful selection of sufficient, valid, and scientifically rigorous data was crucial, to ensure the robustness of the model. In this way, although there may not be as many examples and real data, there are more accessible parameters that the scientific community agrees can serve as indicators [48]. In one of these potentially dangerous regions [7], the danger of abrasion was not decisive but, as concluded in Ref. [22], the potential risk of structural abrasion increases when these criteria are met:

- Low relative humidity (RH) and high wind speeds are present at the same time.
- High total concentrations of suspended particles (TSP) in the air.
- Low percentage of clay [22] ultimately favouring saltation.
- The terrain does not have surface characteristics and is, basically, a vast plain without vegetation or obstacles that serve as barriers to the wind.

Therefore, the critical study factors are: Vegetation (1), Relative Humidity (2), Wind Speed (3), TSP (4) and Soil Composition (5).

On the other hand, despite the lack of studies on the specific problem of wind-blown sand, the effect of this phenomenon on the loss of efficiency of solar panels and other adverse effects has been well-documented. These real cases can help identify locations comprising terrain prone to wind-driven particle movements. However, since the focus of this study is on the wear and tear of metal structures under specific wind and soil conditions, it may not necessarily cause significant degradation of the structures if these

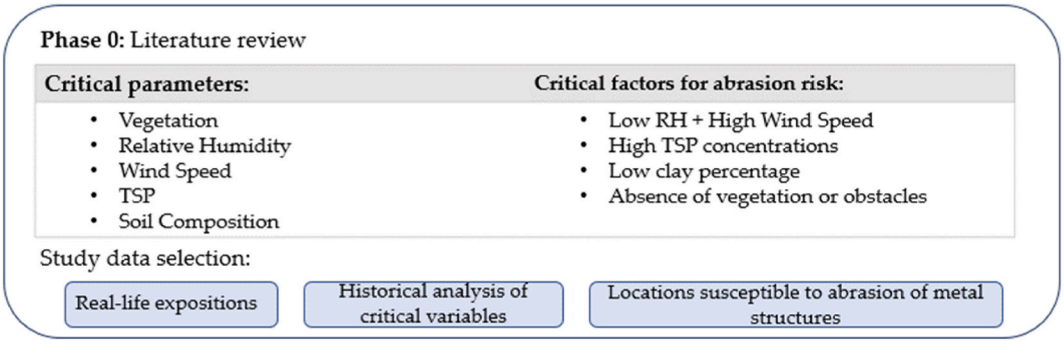

Fig. 2. Process for conducting the initial phase.

conditions are met. Therefore, by reviewing all the study cases presented in the literature and conducting a historical analysis of the main critical variables, it was possible to identify study locations, as examples of areas which are, or are not, susceptible to abrasion, and whether metal structures are likely to suffer from wear and tear.

To sum up, Fig. 2 depicts the entire process required to carry out the first phase. A double verification can be used to select the study data. Firstly, the database was initiated with examples of locations where historical critical data were available, based on expert criteria. Given that climate information is available globally, the selective variable that allows for the delimitation of case studies was total suspended particles. Additionally, all locations with study cases presented in the literature were included and historical information was gathered from all of them, to verify whether they met the rest of the critical factors or not.

2.1.1. Phase 1: input data sources

During this phase, all necessary information was gathered for the model. The sources and types of data were diverse. On the one hand, satellite information, in the form of multispectral images, was required to analyse vegetation and land degradation. On the other hand, information regarding critical variables at the study points, in the form of historical data, was needed. Fig. 3 presents an overview of the different data sources and the processing they underwent.

2.1.1.1. Multispectral images. Multispectral imagery was used to analyse vegetation. Gathering multi-spectral images was performed through different satellites. In this case, images came from the Sentinel-2 fleet, developed by the European Space Agency (ESA) in the framework of the Copernicus project [49]. This fleet consists of two multi-spectral satellites orbiting at 180° offset from each other to obtain images with greater temporal recurrence. Sentinel-2 acquires 13 spectral bands with resolutions of 10–20 and 60 m. In addition, the temporal resolution is either 10 days per satellite or five days combined. The Copernicus Open Access Hub [50] platform allows the images to be downloaded. Subsequently, these images and their bands were processed with the Sentinel Application Platform (SNAP); this allows automatic conversion to surface reflectance or dark object subtraction, among other atmospheric corrections.

After downloading, the images were put together to form a georeferenced mosaic, using the QGIS geographic information system. In this case, the geographic coordinate system SRC EPSG:4326-WGS 84 was used.

2.1.1.2. Critical factors historical data.

– **Wind speed and relative humidity**

Meteorological data corresponding to each study location were downloaded through a third-party service. The study variables were relative humidity and wind speed, and the highest values recorded each hour were taken. For this purpose, HTTP GET type requests were made to the REST API offered by this external web service, whose response contained the requested data in JavaScript Object Notation (JSON) format. The response obtained was adapted and stored for use in subsequent phases. Data were downloaded every hour for a period of one year at each location.

– **Total Suspended Particles**

Likewise, air quality (AQ) data were obtained for such study sites (specifically for suspended particles), taken from the World Air Quality Index Project from EPA (Environmental Protection Agencies, 2022). This is a non-profit project that provides unified, worldwide air quality information from more than 130 countries and covers more than 30,000 stations in 2000 major cities. This information is interesting from a qualitative point of view, as the records of total suspended particulate matter at a given point (taken on a continuous basis, i.e. the annual mean and annual maximum records) can then be understood as an emission source and, therefore, also be considered as one of the criteria above.

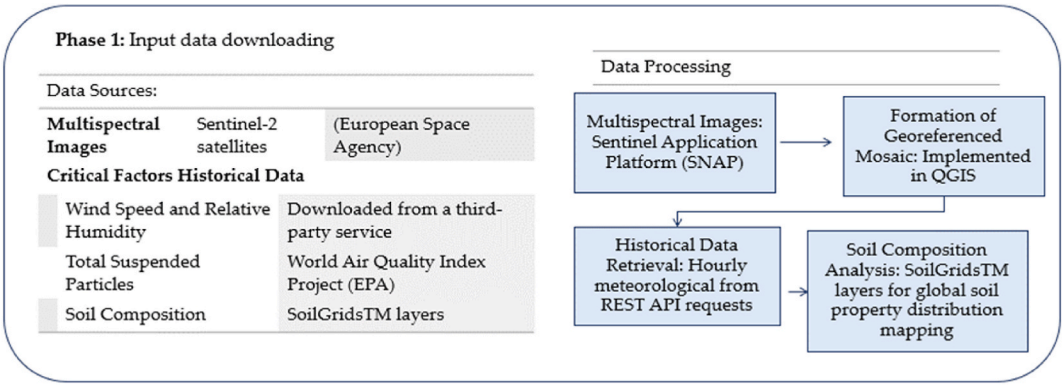

Fig. 3. Methodology details followed during phase 1.

– **Soil composition**

Soil composition was also examined, to analyse its hardness (specifically clay content). For this purpose, one of the SoilGridsTM layers was used [51]. This system for digital soil mapping is based on a global compilation of soil profile data and environmental layers that uses state-of-the-art machine learning methods; the prediction models are fitted using over 230,000 soil profile observations from the WoSIS database [52] and a series of environmental covariates, to map the spatial distribution of soil properties across the globe.

The results from Phase 1, were used to create a mosaic representing all multispectral images with the different bands; all of the critical historical data from the study points were downloaded.

2.1.2. Phase 2: database creation

During this phase, the training dataset was prepared. The training regions should be examples of the sites which are susceptible to abrasion and, therefore, meet the criteria gathered from phase 0. To develop predictive models based on data, the training dataset must be carefully curated and validated. Therefore, a comprehensive methodology is followed to create the dataset (Fig. 4), and the selection of training areas or regions of interest (ROI) is crucial.

These regions of interest were divided into two macro classes, selected individually. A macro class can be composed of different scenarios with different spectral signatures. Since the classification aims to differentiate abrasion susceptible (hereafter SA) from non-abrasion susceptible (hereafter NSA) locations, two main macro classes were distinguished. Within each macro-class, examples were selected to pool all possible variabilities within each study group.

Therefore, the areas were selected by assuming that the susceptible zones (SA) have the following: low relative humidity <50% [53], high wind speeds of >10 m/s [54], high TSP content (1000 μg/m^3) [22], low clay content [22], and low vegetation, based on image classification.

For NSA areas, multiple ROIs were identified, including: water, buildings, areas with different vegetation levels and snow. Thus, different ROIs were obtained for each type of vegetation, different building typologies, various examples of water, rivers, lakes and oceans, as well as snow classes in mountains and glaciers. On the other hand, the scenarios including different degraded soils which are susceptible to abrasion and sand transport, were analysed in another macro class, whose individual examples included different granulometries, soil compositions and moisture contents.

Once all of these ROIs had been determined, they were combined and their spectral signatures analysed to obtain a spectral signature of the set. Subsequently, and as a way of validating the training database, the spectral signatures obtained in each of the examples were verified.

Spectral distance serves to assess the distinguishability of training signatures or pixels, with the aim of identifying whether distinct classes are too similar and, therefore, prone to classification errors.

The Brays Curtis similarity metric [55] was used to evaluate the chosen training data and this ranges from 0 to 100, with zero being totally different and 100 indicating identical values. It is defined by Eq. (1):

$$BC_{ij} = 1 - \frac{2C_{ij}}{S_i + S_j} \tag{1}$$

where C_{ij} is the sum of the lowest values for groups that the two sites have in common and S_i ; S_j are the total number of groups counted at both sites.

After ROIs, the creation and verification of the training set, storing the polygons with the necessary spectral information, was concluded, and the database could be used for classification.

2.1.3. Phase 3: modelling

Finally, the third and last phase consisted of the development and evaluation of the classification model using supervised classification. Fig. 5 provides a simplified representation of the processes followed in this phase.

Semi-automatic classification is an image processing technique that allows the identification of different materials in an image, based on their spectral signature [56]. Because each class has a unique spectral reflectance (spectral signature), the classification exploits the spectral differences to assign each pixel to a class. The process followed consisted of three steps:

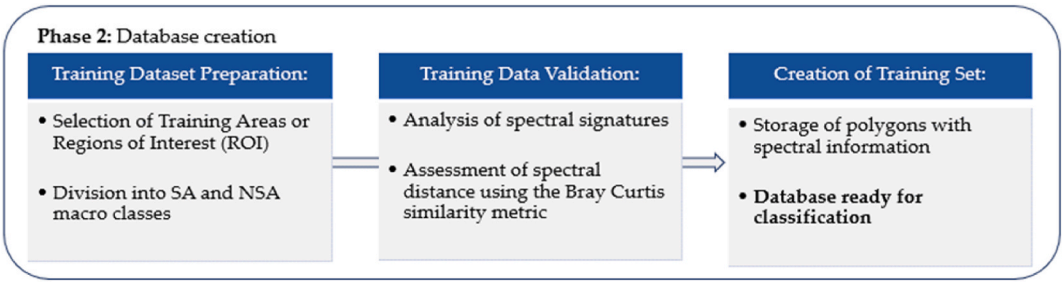

Fig. 4. Process of creating and validating the study database.

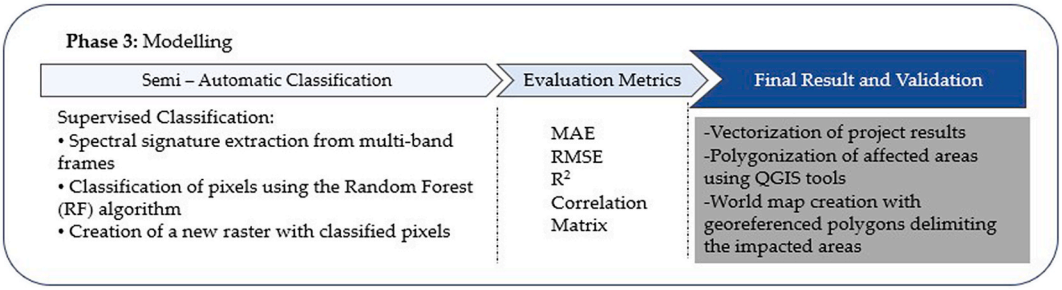

Fig. 5. –Description of the methodology followed during the final phase.

1. The spectral signature of each pixel was extracted from the multi-band frame.
2. The pixel was classified by means of an algorithm.
3. A new raster was created with the classified pixels.

In this case, the chosen algorithm was Random Forest (RF). This is a popular classifier within the remote sensing community, as it can successfully handle high data dimensionality and multicollinearity [57]. This algorithm is a combination of decision trees in which each tree depends on the values of a random vector, tested independently and with the same distribution for each of them [58]. Thus, instead of learning a single model, several models are learned and the estimates from each model are combined. This algorithm has a very good capacity for generalisability because it is both fast and insensitive to overfitting which allows the possibility to validate a model by doing statistical tests. This makes it possible to account for the reliability of the model and is why it has been used in an increasing number of works [59–61].

Different metrics were chosen to evaluate the results of the model:

- Mean absolute error (MAE), which is a common measure to predict the error of a model (Eq. (2)).

$$MAE = \frac{\sum_{i=1}^{N} |y_i - y.M_i|}{N} \tag{2}$$

- Root mean square error (RMSE).

The mean square error is a frequently used measure of the differences between the values predicted by a model and the observed values (Eq. (3)). The smaller the value, the better the performance of the model.

$$RMSE = \sqrt{\frac{\sum_{i=1}^{N} (y_i - y.m_i)^2}{N}} \tag{3}$$

- Determination coefficient.

The coefficient of determination (R^2) is the proportion of the variance of the dependent variable that can be predicted from the independent variables; it is a statistical measure of how close a model is to the actual data points (Eq. (4)). A higher value indicates a better fit between the prediction and the true value.

$$R^2 = 1 - \frac{\sum_{i=1}^{N} (y_i - y.m_i)^2}{\sum_{i=1}^{N} (y_i - y.M_i)^2} \tag{4}$$

Once the final result was obtained and validated, the project results were vectorised and the areas found were then polygonised using the tools available in QGIS to obtain a world map with the georeferenced polygons delimiting the affected areas.

2.1.3.1. Software. The software and versions used were Python 3.8.6, QGIS - SCP 3.16.6 [56], ESA SNAP 9.0.0, and SoilGrids 2020 [62].

3. Results

The outcomes obtained in each of the phases described in the methodology are shown below.

3.1. Literature review

After conducting a comprehensive review of the literature, we identified locations where metallic structures are susceptible to abrasion. Our analysis allowed us to distinguish between areas where terrain degradation may appear to be a potential risk factor for abrasion but where meteorological and granulometric conditions do not result in a significant impact on structures. Annex I presents a list of case studies in which large quantities of sand moved by wind were found to cause energy loss due to the wear or covering of solar panels. However, these studies did not examine the impact of abrasion on metal structures. Nonetheless, these cases helped us to compile a database of areas for which there is a potential risk of abrasion and those where there is not. This is, therefore, taken as an indirect indicator in this study.

3.2. Satellite information

Fig. 6 represents TSP content in each study location as its annual mean value, the larger the point size, the greater the amount of particles. Most study locations with a maximum TSP lower than 1000 μg/m^3 will, therefore, not meet one of the criteria for being SA ROIs.

Moreover, in addition to TSP, wind speed gusts need to be high enough to cause abrasion at each location of interest. Fig. 7 represents the number of hours in which wind speed is higher than 10 m/s, throughout a year. Point size indicates the amount of time that these circumstances existed. It can be seen how different this information is from the TSP content; however, there is no minimum value in this scenario; any period of time with such high wind speeds meets the criteria.

The relationship between these two variables should coincide in time, SA sites being those in which situations where TSP >1000 μg/m^3 and wind gust >10 m/s have occurred.

Regarding relative humidity conditions and soil characteristics, there are clear differences between these variables on an individual basis, as shown in Table 1.

The distribution of values in the study cases, as well as the direct relationship between relative humidity and maximum recorded wind gusts, are displayed in Fig. 8. The colour gradient, from darker to lighter, represents the increasing average relative humidity, while the size of each data point represents the maximum wind speeds, with larger points indicating higher recorded velocities.

3.3. Database creation

The globally available terrain set is classified according to two macroclasses, hence there is large variability. Fig. 9 compares the

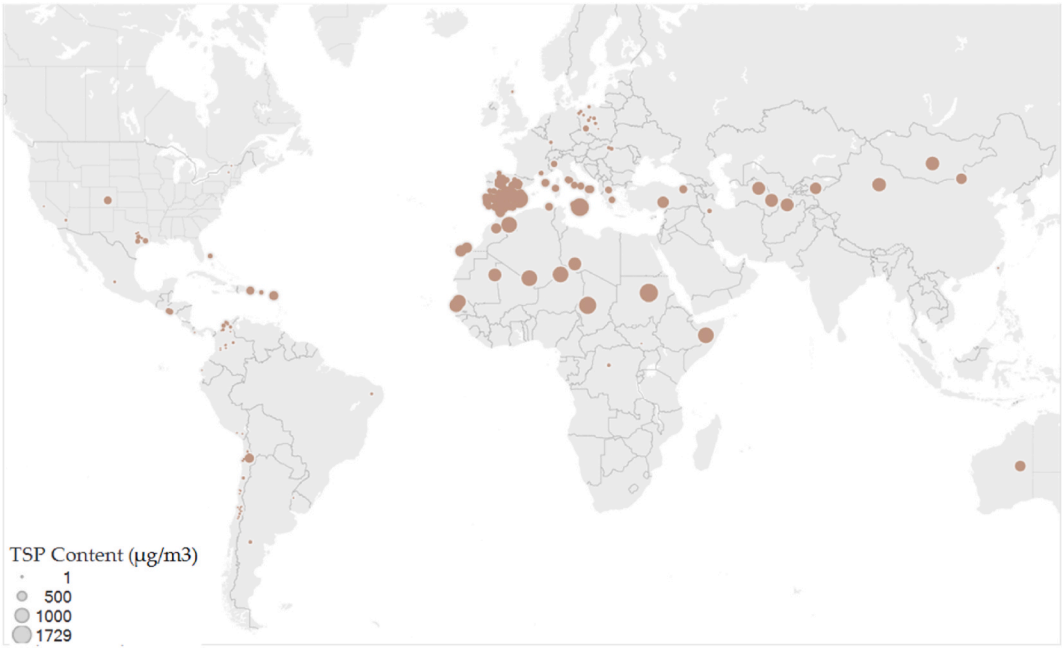

Fig. 6. Maximum Total Suspended Particles content (μg/m^3) at each study location.

Fig. 7. Amount of time (hours) with high wind speed values at each study location.

Table 1
Mean, minimum and maximum of the examples of each class.

	Mean		Min		Max	
	SA	**NSA**	**SA**	**NSA**	**SA**	**NSA**
Relative Humidity (%)	44	78	26	29	96	96
Clay content (g/kg)	161	288	143	150	170	567
Wind Gust (m/s)	17	16	5	5	34	30

spectral signature of the SA macro class (including examples of all the areas susceptible to abrasion) with the NSA macro class. Each of the lines show the average reflectance of that class at each wavelength and the area corresponding to the deviation of that class is shown as an area in the same colour, but lighter. The larger the lighter area, the larger the standard deviation and, therefore, the more heterogeneous the pixels are that form that class. For example, while snow reflects across the whole spectrum, the opposite is true for water; it is precisely those kinds of examples that narrow down the general data in the NSA group.

This spectral variability in the standard deviation is given by both the size of the training area and the variability of the surface area of each class. Since the classification assigns each pixel to a class and pixels are distinguished by their spectral reflectance curves, pixels cannot be distinguished if there is too much spectral overlap. The spectral variability within each class depends on the complexity of the surface type. Therefore, the main difference lies in following the clear pattern observed in SA cases across the whole spectrum.

By analysing the Brays Curtis dissimilarity in some examples of typical scenarios, it was observed that, while some subclasses are perfectly separable (with values lower than 30%), some can conflict with each other, in their separation with the SA zones. Table 2 shows these relationships in the form of a correlation matrix.

The analysis of the spectral signature of vegetation generally depends on various characteristics, such as the type of species being evaluated (leaves, stems, trunk, humidity, etc.), as well as its exposure to different environmental conditions. In the case of deciduous forests, the visible reflectance is low, with an increase in the green colour due to the presence of chlorophyll, which is characteristic of the leaves. Reflectance increases in the near infrared due to low energy absorption by the plants. In the mid-infrared, there is a significant decrease along the wavelengths, as the plant water absorbs energy.

On the other hand, in the case of uncultivated (dry) soils, it is observed that the spectral signature presents a different behaviour: the peak in the green colour of the visible zone is no longer visible and there is an increase in reflectance along the wavelengths, as the plants no longer absorb water. In this case, SA also depends on several characteristics such as air and water content, grain size structure and texture. In this case, when conflicting areas are found, they are either differentiated by colour or by granulometry.

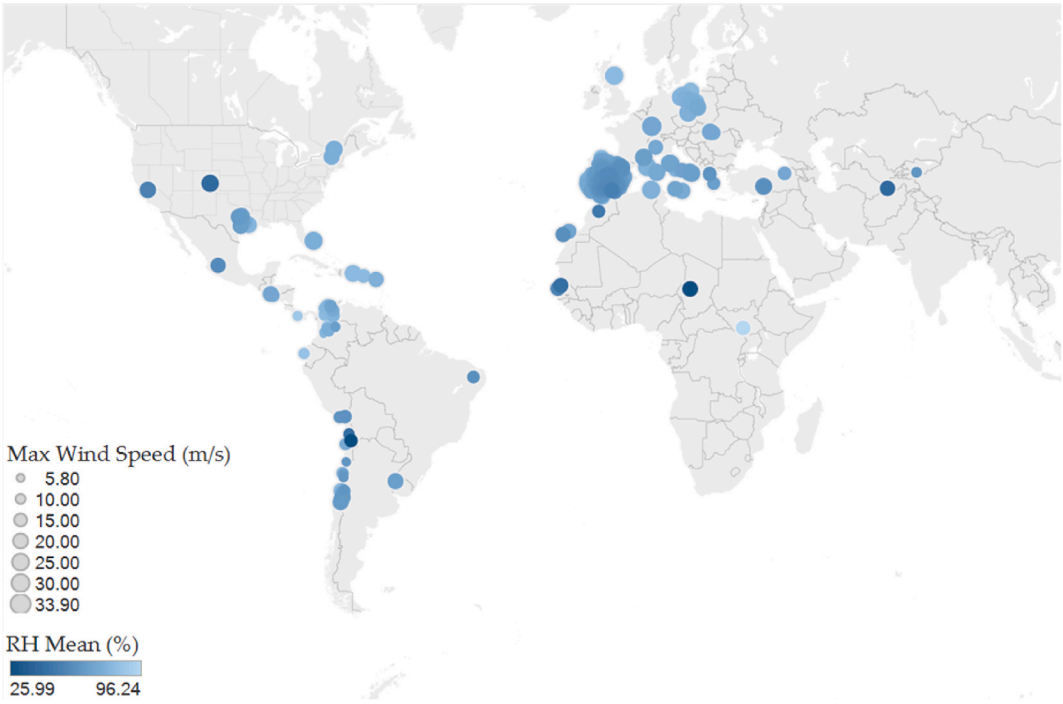

Fig. 8. Distribution of relative humidity and wind speed values in each case.

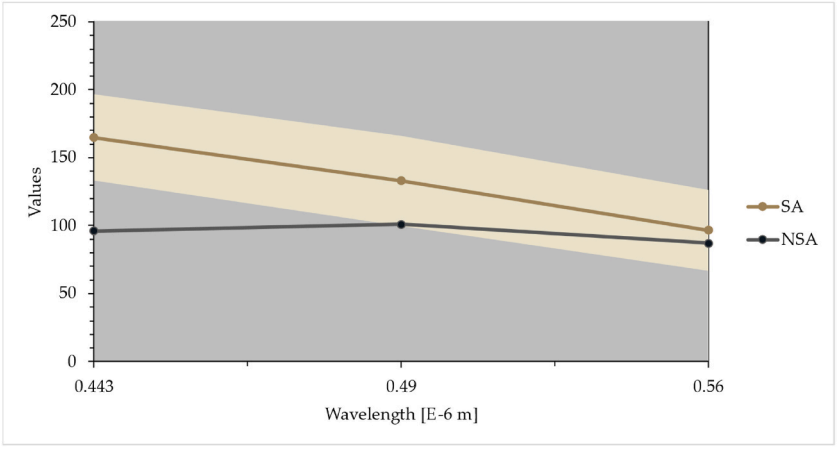

Fig. 9. Spectral signatures of the NSA and SA macro classes.

Table 2
Brays-Curtis similarity (%).

	Water	Snow	Vegetation	Buildings	SA
Water	100.00	16.18	60.48	47.19	28.30
Snow		100.00	21.84	44.36	69.63
Vegetation			100.00	60.15	37.34
Buildings				100.00	69.59
SA					100.00

3.4. Classification

Finally, after the application of the random forest classification algorithm, very satisfactory results were obtained. The main metrics verifying the model fit are summarised in Table 3. After cross-validation of the algorithm, it is observed that a score higher than 98% was obtained for all metrics. A first assessment of the model's performance is the accuracy. This score measures how many labels the model got right out of the total number of predictions, i.e. the percentage of predictions that were correct. Although excessively high values of indicators may be related to over-fitting of this model, given the purpose of this assumption it would not be a disadvantage.

Furthermore, the values of the model errors and model bias show how close the prediction is to the true mean value of an average model.

On the other hand, since accuracy is not a great measure of performance when there are certain imbalances in the classes, more information is added to assess their behaviour in the form of a confusion matrix. Table 4 shows a summary of the classification performed by considering random sampling. It shows that only 0.3% were considered as false negatives and 0.4% as false positives. The rest of the cases were correctly classified in the SA or NSA macro-classes, respectively.

Fig. 10 shows a smaller scale example of the learning result in a dune area on the Canary Islands. On the left is the real multispectral image and, on the right, the classification between NSA and SA areas in yellow. Both macro classes are clearly differentiated and their corresponding georeferenced areas distinguished. It can be seen that the algorithm is able to distinguish different grain sizes or compositions, based not only on their spectral images but also on their deviation results.

After that, as all of the pixels are now perfectly classified, polygons locating the areas susceptible to suffer from wind erosion can be identified. The global results are shown on the world map in Fig. 11.

The QGIS output of the resulting zones, after the application of the model to the case study, is shown in Fig. 12; an overview can be seen on the world map. SA zones are outlined in red, thus limiting both large and small areas. The main zones correspond to the deserts, as expected, but it can be seen that there are many other places. Countries with more variability in their climatic conditions, such as Spain, (which may have many small risk areas), appear in this global-scale figure with numerous delineated zones in red. Conversely, the Sahara Desert, where almost the entire area is considered a risk, has a clearer delineation line around the entire region, with only a few specific non-risk areas marked in the centre.

Once vectorised, the results can be opened on Google Earth and used in any platform, as shown in Fig. 13.

As a result, these georeferenced multipolygons make it easy to determine whether those coordinates are located within an area that is susceptible to and at risk of erosion by windblown sand particles or not, based on a given set of study coordinates. As the Earth's surface is changing [63], the proposed methodology allows the model to be revised at any time, with updated information.

4. Discussion

4.1. Interpretation of results

The results obtained from each phase of the methodology provide valuable insights into the vulnerability of geographic areas to wind abrasion. The literature review helped identify locations where metallic structures are susceptible to abrasion, distinguishing between potential risk areas and those with minimal impact. The compilation of case studies showed on Annex I provided indirect indicators of areas at risk of abrasion.

The analysis of satellite information, including TSP content and wind speed gusts, played a crucial role in determining the criteria for identifying susceptible areas. While TSP levels below 1000 μg/m3 indicated a lower risk of abrasion as indicated in Ref. [22], wind gusts exceeding 10 m/s were essential for potential abrasion. The relationship between these variables, along with relative humidity and soil characteristics, was examined to understand the conditions leading to wind abrasion.

The creation of a scientifically robust database allowed for the classification of terrain into macro classes, highlighting the spectral differences between SA and NSA areas. Spectral signatures of vegetation and uncultivated soils demonstrated distinct patterns, contributing to the classification process. However, some subclasses presented challenges in separating them from SA zones, emphasizing the need for careful analysis and consideration of multiple factors [64,65].

The classification phase utilizing the random forest algorithm, approach already used in different sectors like [66] or [67], yielded highly accurate results, with metrics indicating a model fit above 98%. The accuracy score, along with model errors and bias, provided an assessment of the model's performance. The confusion matrix analysis further confirmed the model's effectiveness in classifying SA and NSA macroclasses, with minimal false negatives and false positives.

4.2. Implications and applications

The findings of this study have significant implications for identifying vulnerable areas prone to wind abrasion. The delineation of

Table 3
Validation variables.

Accuracy	Precision	Correlation	Error rate	RMSE	Bias
0.9922	0.9904	0.9845	0.0078	0.08831	−0.0018

Table 4
Results of the confusion matrix.

		Actual	
		Positive	Negative
Predicted	Positive	True Positive 49.7%	False Positive 0.4%
	Negative	False Negative 0.3%	True Negative 49.6%

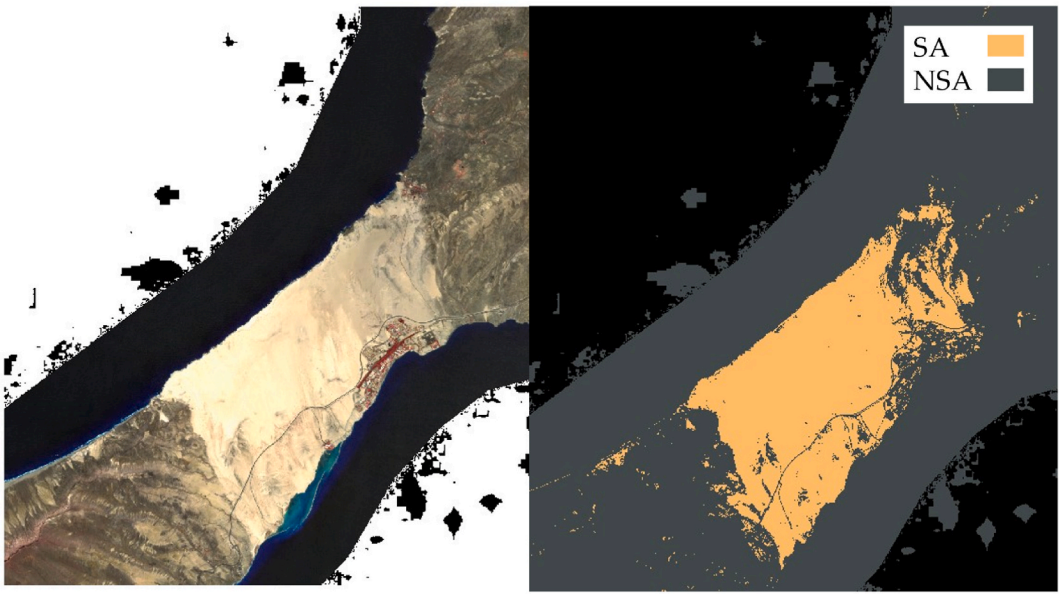

Fig. 10. Example of a degraded soil zone with strong winds and little vegetation.

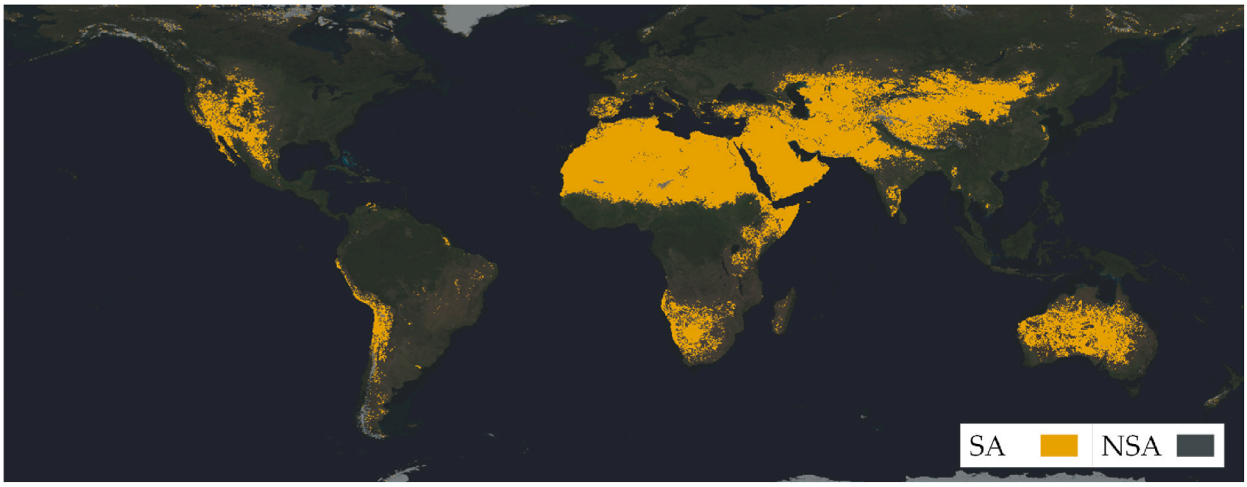

Fig. 11. Global classified map with SA and NSA zones.

SA zones on a global scale, as showcased in the results, allows for a comprehensive understanding of regions at risk. The presence of various risk areas beyond deserts highlights the importance of considering climatic conditions and geographical variability in assessing vulnerability.

The georeferenced multipolygons resulting from the classification process offer practical applications in determining the susceptibility of specific coordinates to wind erosion. The integration of these results into other platforms like Google Earth enhances their

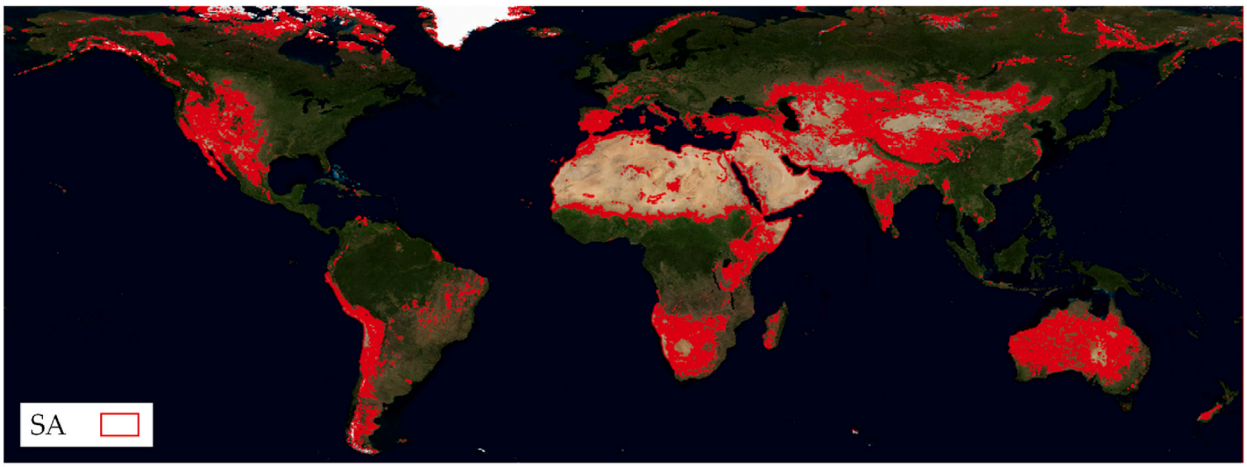

Fig. 12. Classified SA locations, limited as multipolygons and outlined in red.

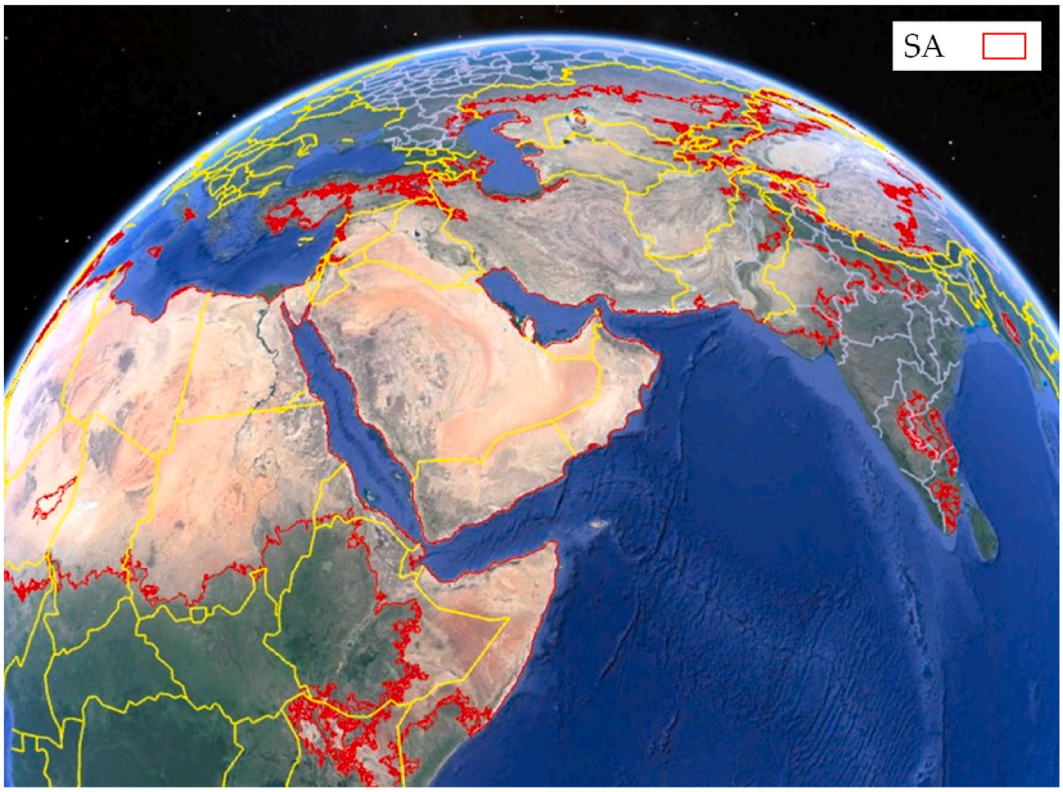

Fig. 13. Vectorised georeferenced multipolygon results in Google Earth.

accessibility and usability for researchers and stakeholders involved in infrastructure design and planning. By increasing the knowledge on material wear caused by particle action and providing insights into the initial design of resilient structures, this research contributes to optimizing infrastructure placement, particularly in the context of renewable energy, where special attention is being paid [42,68]. The proposed hybrid model, incorporating historical data and satellite information, presents a valuable and generalizable approach to addressing the problem of wind abrasion.

4.3. Limitations and future research

It is important to acknowledge the limitations of this study. One limitation is its static nature, as the satellite data and imagery are

representative of a specific study period. Future research could explore the development of a dynamic model that allows for periodic updates, considering temporal variations in wind abrasion vulnerability.

Additional factors, such as wind power and direction, as examined in Ref. [69], can be further investigated. The direction of erosive winds plays a crucial role in determining the origin and path of sand and dust storms originating from arid and semiarid regions [70]. Wind speed is a significant factor in the transportation of sand and dust by wind, which can cause erosion, resulting in the formation of sand dunes and ripples [71]. By expanding the assessment, it is possible to create risk zones applicable to nearby areas. A comprehensive understanding of the phenomenon can be achieved by exploring the interplay between these factors and their impact on susceptibility to wind abrasion.

Furthermore, a pilot case study with an original data set is proposed to validate the obtained results in a real-life scenario. In this way, it is considered interesting to carry out a campaign of real tests that includes the inclusion of samples during long periods of exposure, and whose loss or degradation is measured over time. Likewise, sensors will be included in these locations to determine the value of the study variables and thus provide the additional information necessary for their complete future validation.

5. Conclusions

This paper presents a novel approach to develop a global map for localizing and delimiting areas prone to the degradation of metallic structures caused by windblown particles. The study highlights the specific criteria required for wind erosion to occur, including degraded, dry, and hard terrain with a lack of vegetation, as well as the presence of particles as eroding material and sufficiently strong winds to act as carrier fluid.

While the occurrence of simultaneous high periods of suspended particles and strong winds is relatively rare, it is crucial to note that wind erosion leads to cumulative physical degradation, meaning even short periods of damage are not reversible. Leveraging spectral images and satellite information allows for remote extraction of data and provides additional insights through the analysis of spectral bands. This approach aligns with market expectations and future engineering trends.

The methodology proposed for selecting regions of interest and forming the study database holds vital importance. Furthermore, incorporating additional information and studying influencing variables over extended periods is crucial for comprehensive analysis. The study employs the random forest algorithm as a suitable alternative for semi-automatic classification, achieving a high level of accuracy with less than 1% incorrectly classified pixels during the training phase and an overall accuracy value of 0.9922.

One limitation of the study lies in its static nature, as the satellite data and imagery only represent a specific period under investigation. However, there is a proposal to adapt the model into a dynamic framework that allows for periodic updates, ensuring its relevance over time.

In terms of future research directions, it is suggested to consider incorporating wind power and direction information to create risk zones applicable to adjacent areas. Additionally, conducting a campaign of real tests to validate the obtained results in a real-life scenario is recommended. These future lines of study would enhance the applicability and practicality of the findings, contributing to the field of wind erosion research and its implications for structural integrity and land use planning.

Author contribution statement

Marta Terrados-Cristos: Conceived and designed the experiments; Contributed reagents, materials, analysis tools or data; Wrote the paper.

Francisco Ortega-Fernández: Conceived and designed the experiments; Wrote the paper.

Marina Díaz-Piloñeta: Performed the experiments; Contributed reagents, materials, analysis tools or data.

Vicente Rodríguez Montequín; José Valeriano Álvarez Cabal: Analysed and interpreted the data.

Data availability statement

Data will be made available on request.

Additional information

No additional information is available for this paper.

Funding statement

The results of this research have been funded by the Council of Science, Innovation, and University through FICYT for the realization of R + D + i network projects with grant number AYUD/2021/57,418. Additionally, this work has been funded by the Council of Science, Innovation, and University of the Principality of Asturias with grant number AYUD/2021/50,953.

Declaration of competing interest

The authors declare that they have no known competing financial interests or personal relationships that could have appeared to influence the work reported in this paper.

Annex I.

Location	Source	Type
Acampo, Spain	Private enterprise	Data availability
Acquapendente	ARAP Lazio Agenzia Regionales per la Protezione dell'Ambiente del Lazio	Data availability
Aksu, China	[72]	Case Study
Albisu Uruguay, Latam	Private enterprise	Data availability
Alcochete, Portugal	Private enterprise	Data availability
Aljaval, Spain	Private enterprise	Data availability
Almeria (Spain)	[68]	Case Study
Alto Hospicio, Chile	Sistema Nacional de Calidad del Aire de Chile	Data availability
Angamos Chile, Latam	Private enterprise	Data availability
Angamos, Latam	Private enterprise	Data availability
Antequera, Spain	Private enterprise	Data availability
Apulo, Latam	Private enterprise	Data availability
Arillas	Citizen Project Station 49,570	Data availability
Astudillo, Spain	Private enterprise	Data availability
Atacama Desert (Chile)	[68]	Case Study
Aurora, Latam	Private enterprise	Data availability
Ayteke Bi, Kazakhstan	AirKaz Station 39532416	Data availability
Badajoz, Spain	Private enterprise	Data availability
Balsicas, Spain	Private enterprise	Data availability
Bamako US Embassy, Mali	US EPA	Data availability
Barcience, Spain	Private enterprise	Data availability
Basir, Spain	Private enterprise	Data availability
Bayankhongor, Mongolia	Purple Aire, Station 35,535	Data availability
Bayero University, Kano, Nigeria	Clarity Station 5f21b5f48a16f8060efb498c	Data availability
Beijing, China	[72]	Case Study
Bejaad, EMEA	Private enterprise	Data availability
Belvis, Spain	Private enterprise	Data availability
Beneixama, Spain	Private enterprise	Data availability
Benilde, Spain	Private enterprise	Data availability
Blanca Solar, EMEA	Private enterprise	Data availability
Bobadilla Del Campo, Spain	Private enterprise	Data availability
Bomberos, Chile	Sistema Nacional de Calidad del Aire de Chile	Data availability
Boston, Massachusetts	[73]	Case Study
Boujdour (Morocco)	[74]	Case Study
Brzozowa, Otwock, Mazowieckie, Poland	Regional Inspectorate for Environmental Protection	Data availability
Brzozowa, Otwock, Mazowieckie, Poland	Regional Inspectorate for Environmental Protection	Data availability
Caiquen, Latam	Private enterprise	Data availability

(*continued on next page*)

(*continued*)

Location	Source	Type
Calatrava, Spain	Private enterprise	Data availability
Caldas, Colombia	Área Metropolitana del Valle de Aburrá	Data availability
California, United States	[75]	Case Study
Campano, Latam	Private enterprise	Data availability
Canal Del Dique, Latam	Private enterprise	Data availability
Cannes Brousailles	L'observatoire de Qualité de l'Air en región sud Provence Alpes côté d'azur	Data availability
Cantalapiedra, Spain	Private enterprise	Data availability
Cardenal, Latam	Private enterprise	Data availability
Carpio, Spain	Private enterprise	Data availability
Carrasquilla, Spain	Private enterprise	Data availability
Carregado, Portugal	Private enterprise	Data availability
Cassino	ARAP Lazio Agenzia Regionales per la Protezione dell'Ambiente del Lazio	Data availability
Celeste, Italy	Private enterprise	Data availability
Celso, Spain	Private enterprise	Data availability
Centauro, Spain	Private enterprise	Data availability
Centro Quintero, Chile	Sistema Nacional de Calidad del Aire de Chile	Data availability
Cesaredas, Portugal	Private enterprise	Data availability
Chacon, Latam	Private enterprise	Data availability
Chajnantor (Chile)	[68]	Case Study
Changhua Taiwan, EMEA	Private enterprise	Data availability
Chiaramonte I, EMEA	Private enterprise	Data availability
Chiaramonte, Italy	Private enterprise	Data availability
Chiloe Chile, Latam	Private enterprise	Data availability
Chiloe, Latam	Private enterprise	Data availability
Choroy, Latam	Private enterprise	Data availability
Cicliano, Italy	Private enterprise	Data availability
Cienaga, Latam	Private enterprise	Data availability
Colores, Spain	Private enterprise	Data availability
Corral Pocket, Utah	[76]	Case Study
Corso Chile, Latam	Private enterprise	Data availability
Corso, Latam	Private enterprise	Data availability
Crucero, California	[76]	Case Study
Cruz De Hierro, Spain	Private enterprise	Data availability
Dos Hermanas, Spain	Private enterprise	Data availability
Dubhuang, China	[72]	Case Study
Dugout Ranch, Utah	[76]	Case Study
Durango, MExico	INECC Instituto Nacional de Ecología y Cambio Climático	Data availability
Egypt	[77]	Case Study

(*continued on next page*)

(*continued*)

Location	Source	Type
El Aromo, Latam	Private enterprise	Data availability
El Ejido, Spain	Consejería de Medio ambiente y Ordenación. Junta de Andalucía & European Environment Agency	Data availability
El Encinar, Spain	Private enterprise	Data availability
El Lauredal, Asturias, Spain	Monitorización Red de Calidad del Aire del Principado de Asturias	Data availability
El Loro Choroy, Latam	Private enterprise	Data availability
El Maillo, Salamanca, Spain	European Environment Agency | Junta Castilla y León	Data availability
El Picarral	Ayuntamiento de Zaragoza. La Ciudad Medio Ambiente	Data availability
El Tomillar, Spain	Private enterprise	Data availability
El-Kharga, Egipto	[42]	Case Study
Elvisa, Spain	Private enterprise	Data availability
Eme F, Chile	Sistema Nacional de Calidad del Aire de Chile	Data availability
Erfoud (Morocco)	[22]	Case Study
Escuadrón, ENESA, Chile	Sistema Nacional de Calidad del Aire de Chile	Data availability
Escuderos, Spain	Private enterprise	Data availability
Ferentino	ARAP Lazio Agenzia Regionales per la Protezione dell'Ambiente del Lazio	Data availability
Gandesa, Spain	Medi Ambient. Generalitat de Catalunya & European Environment Agency	Data availability
Garcimunoz, Spain	Private enterprise	Data availability
Gaviotin, Latam	Private enterprise	Data availability
Gobi Desert	[78]	Case Study
Gobi Desert	[79]	Case Study
Gobi Desert	[80]	Case Study
Gobi Desert	[81]	Case Study
Gran Canaria Iii, EMEA	Private enterprise	Data availability
Gran Teno, Latam	Private enterprise	Data availability
Granada, Spain	Consejería de Medio ambiente y Ordenación. Junta de Andalucía & European Environment Agency	Data availability
Granollers, Spain	Medi Ambient. Generalitat de Catalunya & European Environment Agency	Data availability
Grecia Agios Christophoros, EMEA	Private enterprise	Data availability
Guadelopupe, France	Association Agréée de Surveillance de la Qualité de l'Air de Guadeloupe	Data availability
Guillena, Spain	Consejería de Medio ambiente y Ordenación. Junta de Andalucía & European Environment Agency	Data availability
Gujarat (India)	[82]	Case Study
Hefei, China	[72]	Case Study
Hermod, Spain	Private enterprise	Data availability
Honda, Latam	Private enterprise	Data availability
Huatacondo, Latam	Private enterprise	Data availability
Igualada, Spain	Medi Ambient. Generalitat de Catalunya & European Environment Agency	Data availability
Independencia, Latam	Private enterprise	Data availability
Jerez, Spain	Consejería de Medio ambiente y Ordenación. Junta de Andalucía & European Environment Agency	Data availability
Jumilla, Spain	Private enterprise	Data availability
Kalgoorlie, Australia	Western Australia Air Quality Management Branch	Data availability

(*continued on next page*)

(*continued*)

Location	Source	Type
Kayseri, EMEA	Private enterprise	Data availability
Koscierzyna, Poland	Regional Inspectorate for Environmental Protection	Data availability
Kozani, EMEA	Private enterprise	Data availability
Kyrgyzstan	Bishkek Air Quality Monitor – US Embassy	Data availability
La Encantada, Spain	Private enterprise	Data availability
La Francesca, Italy	Private enterprise	Data availability
La Loma, Latam	Private enterprise	Data availability
La Mata, Latam	Private enterprise	Data availability
La Paz, Latam	Private enterprise	Data availability
La Tolua, Latam	Private enterprise	Data availability
La Union, Latam	Private enterprise	Data availability
La Victoria, Latam	Private enterprise	Data availability
Laâyoune (Morocco)	[74]	Case Study
Lanzhou-Xinjiang Railway	[83]	Case Study
Las Lomillas, Spain	Private enterprise	Data availability
Las Vaguadas, Spain	Private enterprise	Data availability
Laverne, Spain	Private enterprise	Data availability
Lepanto, Spain	Consejería de Medio ambiente y Ordenación. Junta de Andalucía & European Environment Agency	Data availability
Leucade, Greece	[23]	Case Study
Libya desert	[77]	Case Study
Llano Grande, Latam	Private enterprise	Data availability
Llanos Pelaos, EMEA	Private enterprise	Data availability
Lo Chacon, Latam	Private enterprise	Data availability
Lo Miguel, Latam	Private enterprise	Data availability
Los Santos, EMEA	Private enterprise	Data availability
Loutsa, EMEA	Private enterprise	Data availability
Lucainena, Spain	Private enterprise	Data availability
Lupi, Latam	Private enterprise	Data availability
Manlleu, Spain	Medi Ambient. Generalitat de Catalunya & European Environment Agency	Data availability
Manzanares, Spain	Private enterprise	Data availability
Marigot, France	Association Agréée de Surveillance de la Qualité de l'Air de Guadeloupe	Data availability
Matarani, Latam	Private enterprise	Data availability
Meca, Saudi Arabia	[32]	Case Study
Medina, Saudi Arabia	[33]	Case Study
Michilla Chile, Latam	Private enterprise	Data availability
Minas De Orgueirel, Portugal	Private enterprise	Data availability
Missour (Morocco)	[68]	Case Study
Mollet, Spain	Medi Ambient. Generalitat de Catalunya & European Environment Agency	Data availability

(*continued on next page*)

(*continued*)

Location	Source	Type
Montechoro, Portugal	Private enterprise	Data availability
Montsec, Spain	Medi Ambient. Generalitat de Catalunya & European Environment Agency	Data availability
Moratalla, Spain	Private enterprise	Data availability
Morgavel, Portugal	Private enterprise	Data availability
Moroco	[84]	Case Study
Moroco	[85]	Case Study
Moroco	[22]	Case Study
Moroco	[22]	Case Study
Moroco	[22]	Case Study
Msida	European Environmental Agency & ERA	Data availability
Nagoya, Japan	[72]	Case Study
Naha, Japan	[72]	Case Study
Naipes, Spain	Private enterprise	Data availability
Nascita, Italy	Private enterprise	Data availability
Naves, EMEA	Private enterprise	Data availability
Nobsa I, Latam	Private enterprise	Data availability
Nobsa, Latam	Private enterprise	Data availability
Norfolk, UK	[86]	Case Study
Noroccidental Egypt	[28]	Case Study
North Soda Lake, California	[76]	Case Study
Odeillo (France)	[68]	Case Study
Olivenza, Spain	Private enterprise	Data availability
Olivenza, Spain	Private enterprise	Data availability
Ouarzazate (Morocco)	[74]	Case Study
Ouarzazate (Morocco)	[68]	Case Study
Palmela, Portugal	Private enterprise	Data availability
Pangui, Latam	Private enterprise	Data availability
Patras, Greece	[87]	Case Study
Peñaflor, Spain	Private enterprise	Data availability
Peñaflor Chile, Latam	Private enterprise	Data availability
Perafort, Spain	Medi Ambient. Generalitat de Catalunya & European Environment Agency	Data availability
Peralta, Spain	Private enterprise	Data availability
Pessegueiro, Portugal	Private enterprise	Data availability
Petalo De Magdalena, Latam	Private enterprise	Data availability
Pitarco, Spain	Private enterprise	Data availability
Plaza Elíptica, Madrid, Spain	Calidad del Aire en Madrid, Servicio de Protección de la Atmósfera	Data availability
Popayán, Colombia	Área Metropolitana del Valle de Aburrá	Data availability
Porton Del Sol, Latam	Private enterprise	Data availability
Prisca, Spain	Private enterprise	Data availability
Puerta De Sol, Spain	Private enterprise	Data availability
Puerto Plata, Dominican Republic	Citizen Science Project Station 249	Data availability
Qinjdao, China	[72]	Case Study

(*continued on next page*)

(*continued*)

Location	Source	Type
Quebrada De Talca Chile, Latam	Private enterprise	Data availability
Quilicura, Chile	Sistema Nacional de Calidad del Aire de Chile	Data availability
Qujing, China	World Air Quality Index Project	Data availability
Radona, Spain	Private enterprise	Data availability
Rajasthan (India)	[82]	Case Study
Ricobayo, Spain	Private enterprise	Data availability
Rimini, Latam	Private enterprise	Data availability
Rinaldone, Italy	Private enterprise	Data availability
Rinnovabili, Italy	Private enterprise	Data availability
Romeralejo, Spain	Consejería de Medio ambiente y Ordenación. Junta de Andalucía & European Environment Agency	Data availability
Salamanca Chile, Latam	Private enterprise	Data availability
Salamanca, Latam	Private enterprise	Data availability
Salinas, Spain	Private enterprise	Data availability
Sambuca, EMEA	Private enterprise	Data availability
Sambuca, Italy	Private enterprise	Data availability
San Cristobal, Colombia	Área Metropolitana del Valle de Aburrá	Data availability
San Felipe, Latam	Private enterprise	Data availability
San Fernando, Spain	Private enterprise	Data availability
San Fernando, Spain	Consejería de Medio ambiente y Ordenación. Junta de Andalucía & European Environment Agency	Data availability
San Luis, Argentina	Citizen Science Project Station 63,898	Data availability
San Mateo, Mexico	INECC Instituto Nacional de Ecología y Cambio Climático	Data availability
San Salvador, El Salvador	Ministerio de Medio Ambiente y Recursos Naturales (MARN) de Salvador	Data availability
Santa Maria, Brazil	Citizen Science Project Station 70,735	Data availability
Santeramo, Italy	Private enterprise	Data availability
Santiago de Cali, Colombia	Área Metropolitana del Valle de Aburrá	Data availability
Saravena, Colombia	Área Metropolitana del Valle de Aburrá	Data availability
Seoul, South Korea	[72]	Case Study
Sherabad, EMEA	Private enterprise	Data availability
Skoura (Morocco)	[74]	Case Study
south of Algeria.	[88]	Case Study
Southeast Asia	[89]	Case Study
St Kitt Island, Latam	Private enterprise	Data availability
Sta Lucia, Latam	Private enterprise	Data availability
Suluova Turkey	Air Qualtity Index Project	Data availability
Szczecinek ul. Przemyslowa, Poland	Regional Inspectorate for Environmental Protection	Data availability
Tabernas (Spain)	[68]	Case Study
Tabernasacero, Spain	Private enterprise	Data availability
Tabua, Portugal	Private enterprise	Data availability

(*continued on next page*)

(*continued*)

Location	Source	Type
Taklimakan desert, China	[72]	Case Study
Talayuela, Spain	Private enterprise	Data availability
Talca, Latam	Private enterprise	Data availability
Tarifa, Spain	Private enterprise	Data availability
Tarim Basin China	[90]	Case Study
Tarragona, Spain	Medi Ambient. Generalitat de Catalunya & European Environment Agency	Data availability
Temara (Morocco)	[74]	Case Study
Temara (Morocco)	[68]	Case Study
Terracina, Italy	Private enterprise	Data availability
The Gap, Australia	Air quality. Environment, land and water. Queensland Government	Data availability
Tolva, Latam	Private enterprise	Data availability
Torneo, Spain	Consejería de Medio ambiente y Ordenación. Junta de Andalucía & European Environment Agency	Data availability
Torrubias, Spain	Private enterprise	Data availability
Toulon Claret	L'observatoire de Qualité de l'Air en región sud Provence Alpes côté d'azur	Data availability
Tucsia, Italy	Private enterprise	Data availability
Tulua, Latam	Private enterprise	Data availability
Valdecarretas, Spain	Private enterprise	Data availability
Valencia De Las Torres, Spain	Private enterprise	Data availability
Vas Cicliano, EMEA	Private enterprise	Data availability
Velilla, Spain	Private enterprise	Data availability
Ventus Colombia, Latam	Private enterprise	Data availability
Villacastin, Spain	Private enterprise	Data availability
Villafranca De Barros, Spain	Private enterprise	Data availability
Villanueva Del Rey, Spain	Private enterprise	Data availability
Villareal, Spain	Private enterprise	Data availability
Wloclawek-Okrzei, Poland	Regional Inspectorate for Environmental Protection	Data availability
Wroclaw – Korzeniowskiego, Poland	Regional Inspectorate for Environmental Protection	Data availability
Zafra, Spain	Private enterprise	Data availability
Zagora (Morocco)	[22]	Case Study
Zagora (Morocco)	[91]	Case Study
Zamora, Spain	Private enterprise	Data availability
Zenete, Spain	Private enterprise	Data availability
Zhangye City, China.	[83]	Case Study
Zielona Góra, Poland	Regional Inspectorate for Environmental Protection	Data availability
Znamensk, Russia	Citizen Science project Station 39,514	Data availability
Zračna luka Dubrovnik	Croatian Environment Agency	Data availability

References

[1] Y. Liu, et al., Life-cycle maintenance strategy of bridges considering reliability, environment, cost and failure probability CO2 emission reduction: a bridge study with climate scenarios, J. Clean. Prod. 379 (Dec. 2022), 134740, https://doi.org/10.1016/j.jclepro.2022.134740.

[2] Z. Luo, B. Yang, Towards resilient and smart urban road networks: connectivity restoration via community structure, Sustain. Cities Soc. 75 (Dec. 2021), 103344, https://doi.org/10.1016/j.scs.2021.103344.

[3] 'Part I: general aspects of corrosion, corrosion control, and corrosion prevention', in *corrosion atlas case studies*, in: F. Khoshnaw, R. Gubner (Eds.), Corrosion Atlas Series, Elsevier, 2020, https://doi.org/10.1016/B978-0-12-818760-9.02002-X xxv–xli.

[4] B. Gobereit, L. Amsbeck, M. Ebert, Abrasion, Corrosion and Erosion of Particles and Metallic Structure in Solid Particle Receivers, Jan. 2016.

[5] E. Kusmierek, E. Chrzescijanska, Atmospheric corrosion of metals in industrial city environment, Data Brief 3 (Jun. 2015) 149–154, https://doi.org/10.1016/j.dib.2015.02.017.

[6] Y.-Z. Xu, Zhou Liu, Tan Wang, Huang, An overview of major experimental methods and apparatus for measuring and investigating erosion-corrosion of ferrous-based steels, Metals 10 (Jan. 2020) 180, https://doi.org/10.3390/met10020180.

[7] L. Raffaele, L. Bruno, Windblown sand action on civil structures: definition and probabilistic modelling, Eng. Struct. 178 (Jan. 2019) 88–101, https://doi.org/10.1016/j.engstruct.2018.10.017.

[8] J.F. Kok, E.J.R. Parteli, T.I. Michaels, D.B. Karam, The physics of wind-blown sand and dust, Rep. Prog. Phys. Phys. Soc. G. B. 75 (10) (Oct. 2012), 106901, https://doi.org/10.1088/0034-4885/75/10/106901.

[9] Y.P. Shao, M.R. Raupach, J.F. Leys, A model for predicting aeolian sand drift and dust entrainment on scales from paddock to region, Soil Res. 34 (3) (1996) 309–342, https://doi.org/10.1071/sr9960309.

[10] A. Klik, Wind Erosion Assessment in Austria Using Wind Erosion Equation and GIS, Proceddings OECD Expert Meet, *Rome*, Jan, 2004.

[11] M. Jarrah, S. Mayel, J. Tatarko, R. Funk, K. Kuka, A review of wind erosion models: data requirements, processes, and validity, Catena 187 (Apr. 2020), 104388, https://doi.org/10.1016/j.catena.2019.104388.

[12] B. Liu, J. Qu, D. Ning, Q. Han, D. Yin, P. Du, WECON: a model to estimate wind erosion from disturbed surfaces, Catena 172 (Jan. 2019) 266–273, https://doi.org/10.1016/j.catena.2018.08.037.

[13] H. Arabnejad, A. Mansouri, S. Shirazi, B. McLaury, Evaluation of Solid Particle Erosion Equations and Models for Oil and Gas Industry Applications, Jan. 2015, https://doi.org/10.2118/174987-MS.

[14] S. Shirazi, B. McLaury, H. Arabnejad, A Semi-mechanistic Model for Predicting Sand Erosion Threshold Velocities in Gas and Multiphase Flow Production, Sep. 2016, https://doi.org/10.2118/181487-MS.

[15] B. Omar, M.H. Mohammed, Z. Azari, A. Sorour, N. Merah, P. Guy, Effect of sandblasting on tensile properties, hardness and fracture resistance of a line pipe steel used in Algeria for oil transport, J. Fail. Anal. Prev. (Aug. 2017) 1–15, https://doi.org/10.1007/s11668-017-0313-4.

[16] A. Asgharpour, P. Zahedi, H. Khanouki, S. Shirazi, B. McLaury, Experimental investigation of solid particle erosion in successive elbows in gas dominated flows, J. Fluid Eng. 142 (Jun) (2020), https://doi.org/10.1115/1.4046109.

[17] H.A. Khanouki, Development of Erosion Equations for Solid Particle and Liquid Droplet Impact, University of Tulsa, 2015. *Ph.D. Dissertation*.

[18] A. Mansouri, A Combined CFD-Experimental Method for Developing an Erosion Equation for Both Gas-Sand and Liquid-Sand Flows, THE UNIVERSITY OF TULSA THE GRADUATE SCHOOL, 2016.

[19] H. Yun-Hong, X. Yong-Ming, Reserch on the mechanical-properties of flexible surface-material by erosion in Sandstorm-Environment, 2010 Int. Conf. Mech. Autom. Control Eng. MACE2010 (Jun. 2010), https://doi.org/10.1109/MACE.2010.5536772.

[20] A. Bahri, N. Guermazi, K. Elleuch, M. Ürgen, On the erosive wear of 304L stainless steel caused by olive seed particles impact: modeling and experiments, Tribol. Int. 102 (Oct. 2016) 608–619, https://doi.org/10.1016/j.triboint.2016.06.020.

[21] C. Mele, F. Lionetto, B. Bozzini, 'An erosion-corrosion investigation of coated steel for applications in the oil and gas field, based on bipolar electrochemistry', Coatings 10 (2) (Feb. 2020) 92, https://doi.org/10.3390/coatings10020092.

[22] F. Wiesinger, et al., Sandstorm erosion on solar reflectors: highly realistic modeling of artificial aging tests based on advanced site assessment, Appl. Energy 268 (Jun. 2020), 114925, https://doi.org/10.1016/j.apenergy.2020.114925.

[23] R. Mehdipour, Z. Baniamerian, A new approach in reducing sand deposition on railway tracks to improve transportation, Aeolian Res 41 (Dec. 2019), 100537, https://doi.org/10.1016/j.aeolia.2019.07.003.

[24] L. Bruno, M. Horvat, L. Raffaele, Windblown sand along railway infrastructures: a review of challenges and mitigation measures, J. Wind Eng. Ind. Aerod. 177 (Jun. 2018) 340–365, https://doi.org/10.1016/j.jweia.2018.04.021.

[25] L. Bruno, M. Horvat, L. Raffaele, Windblown sand along railway infrastructures: a review of challenges and mitigation measures, J. Wind Eng. Ind. Aerod. 177 (Jun. 2018) 340–365, https://doi.org/10.1016/j.jweia.2018.04.021.

[26] X. Cao, et al., Sand particle erosion resistance of the multilayer gradient TiN/Ti coatings on Ti6Al4V alloy, Surf. Coat. Technol. 365 (May 2019) 214–221, https://doi.org/10.1016/j.surfcoat.2018.08.066.

[27] H. Nomoto, 10 - solid particle erosion analysis and protection design for steam turbines, in: T. Tanuma (Ed.), Advances in Steam Turbines for Modern Power Plants, Woodhead Publishing, 2017, pp. 219–239, https://doi.org/10.1016/B978-0-08-100314-5.00010-5.

[28] Y.M. El-Sherbiny, 'Erosive wear of different facade finishing materials', HBRC J 14 (3) (Dec. 2018) 431–437, https://doi.org/10.1016/j.hbrcj.2018.04.001.

[29] M.L. Martínez, N.P. Psuty, Coastal Dunes, Springer, 2004.

[30] P.G. Fookes, E.M. Lee, Desert environments: landscapes and stratigraphy, Geol. Today 25 (5) (2009) 172–180, https://doi.org/10.1111/j.1365-2451.2009.00722.x.

[31] L. Raffaele, L. Bruno, Windblown sand action on civil structures: definition and probabilistic modelling, Eng. Struct. 178 (Jan. 2019) 88–101, https://doi.org/10.1016/j.engstruct.2018.10.017.

[32] CEIT, 'Ceit-IK4 colabora en un nuevo carril para el Ave del desierto ante la abrasión que crea la arena al cumplir los primeros 1000 viajes', May 28, 2019 [Online]. Available: https://www.ceit.es/es/.

[33] I.A. Carrascal, J.A. Casado, S. Diego, J.A. Polanco, Dynamic behaviour of high-speed rail fastenings in the presence of desert sand, Construct. Build. Mater. 117 (Aug. 2016) 220–228, https://doi.org/10.1016/j.conbuildmat.2016.05.023.

[34] S. Corti, F. Molteni, T.N. Palmer, Signature of recent climate change in frequencies of natural atmospheric circulation regimes, Nature 398 (6730) (Apr. 1999) 799–802, https://doi.org/10.1038/19745.

[35] V. Sissakian, N. Al-Ansari, S. Knutsson, Sand and dust storm events in Iraq, Nat. Sci. 5 (Jan. 2013) 1084–1094, https://doi.org/10.4236/ns.2013.510133.

[36] Y. Chen, Flood hazard zone mapping incorporating geographic information system (GIS) and multi-criteria analysis (MCA) techniques, J. Hydrol. 612 (Sep. 2022), 128268, https://doi.org/10.1016/j.jhydrol.2022.128268.

[37] G.A. Yousef, M.A. Elazony, A. Abdelsattar, M.M. Sewailam, O.H. Elsaid, Applying an integrated remote sensing-GIS approach in the documentation of handicraft centers at new valley governorate, Egypt, Egypt. J. Remote Sens. Space Sci. 25 (3) (Dec. 2022) 731–739, https://doi.org/10.1016/j.ejrs.2022.04.004.

[38] F. Fang, et al., Spatial context-aware method for urban land use classification using street view images, ISPRS J. Photogrammetry Remote Sens. 192 (Oct. 2022) 1–12, https://doi.org/10.1016/j.isprsjprs.2022.07.020.

[39] O.M. Sorkhabi, B. Shadmanfar, E. Kiani, Monitoring of dam reservoir storage with multiple satellite sensors and artificial intelligence, Results Eng (Jul. 2022), 100542, https://doi.org/10.1016/j.rineng.2022.100542.

[40] H.G. Kuma, F.F. Feyessa, T.A. Demissie, Land-use/land-cover changes and implications in Southern Ethiopia: evidence from remote sensing and informants, Heliyon 8 (3) (Mar. 2022), e09071, https://doi.org/10.1016/j.heliyon.2022.e09071.

[41] Md J. Faruque, et al., Monitoring of land use and land cover changes by using remote sensing and GIS techniques at human-induced mangrove forests areas in Bangladesh, Remote Sens. Appl. Soc. Environ. 25 (Jan. 2022), 100699, https://doi.org/10.1016/j.rsase.2022.100699.

[42] H.A. Megahed, A. Hassoup, A.E.-H.A. Farrag, D. Wahba, Modeling the environmental hazards of el-kharga oasis sand dunes, western desert of Egypt, using remote sensing and GIS techniques: research article- DOI: 10.23953/cloud.ijarsg.505, Int. J. Adv. Remote Sens. GIS 10 (1) (Jul. 2021). Art. no. 1.
[43] M. Ferrari, F. Cirisano, High transmittance and highly amphiphobic coatings for environmental protection of solar panels, Adv. Colloid Interface Sci. 286 (Dec. 2020), 102309, https://doi.org/10.1016/j.cis.2020.102309.
[44] A. Almajed, K. Lemboye, M.G. Arab, A. Alnuaim, Mitigating wind erosion of sand using biopolymer-assisted EICP technique, Soils Found. 60 (2) (Apr. 2020) 356–371, https://doi.org/10.1016/j.sandf.2020.02.011.
[45] H. Meng, Y. Gao, J. He, Y. Qi, L. Hang, Microbially induced carbonate precipitation for wind erosion control of desert soil: field-scale tests, Geoderma 383 (Feb. 2021), 114723, https://doi.org/10.1016/j.geoderma.2020.114723.
[46] Y. Shi, Z.M. Shi, Ultrasonic surface treatment for improving wind-blown sand erosion resistance of cementitious materials, Wear 460–461 (Nov. 2020), 203185, https://doi.org/10.1016/j.wear.2020.203185.
[47] H. Arabnejad, A. Mansouri, S.A. Shirazi, B.S. McLaury, Development of mechanistic erosion equation for solid particles, Wear 332 (333) (May 2015) 1044–1050, https://doi.org/10.1016/j.wear.2015.01.031.
[48] F. Wiesinger, et al., Assessment of the erosion risk of sandstorms on solar energy technology at two sites in Morocco, Sol. Energy 162 (Mar. 2018) 217–228, https://doi.org/10.1016/j.solener.2018.01.004.
[49] Programme of the European Union, 'Copernicus | EUROPE'S EYES ON EARTH'. [Online]. Available: https://www.copernicus.eu/en.
[50] ESA European Commission, 'Copernicus Open Access Hub'. [Online].
[51] M. Duan, X. Song, X. Liu, D. Cui, X. Zhang, Mapping the soil types combining multi-temporal remote sensing data with texture features, Comput. Electron. Agric. 200 (Sep. 2022), 107230, https://doi.org/10.1016/j.compag.2022.107230.
[52] WoSIS Soil Profile Database'. Accessed: January. 17, 2023. [Online]. Available: https://www.isric.org/explore/wosis.
[53] World Meteorological Organization, 'World Weather Information Service'. [Online]. Available:https://worldweather.wmo.int/.
[54] A. E. de Meteorología, 'Agencia Estatal de Meteorología | Gobierno de España'. [Online]. Available:https://www.aemet.es/.
[55] J.R. Bray, J.T. Curtis, An ordination of the upland forest communities of southern Wisconsin, Ecol. Monogr. 27 (4) (1957) 326–349.
[56] L. Congedo, Semi-Automatic Classification Plugin User Manual, 2014, https://doi.org/10.13140/RG.2.1.1219.3524.
[57] M. Belgiu, L. Drăguţ, Random forest in remote sensing: a review of applications and future directions, ISPRS J. Photogrammetry Remote Sens. 114 (Apr. 2016) 24–31, https://doi.org/10.1016/j.isprsjprs.2016.01.011.
[58] X. Yu, Q. Zeng, Random forest algorithm-based classification model of pesticide aquatic toxicity to fishes, Aquat. Toxicol. 251 (Oct. 2022), 106265, https://doi.org/10.1016/j.aquatox.2022.106265.
[59] Y. Loozen, et al., Mapping canopy nitrogen in European forests using remote sensing and environmental variables with the random forests method, Remote Sens. Environ. 247 (Sep. 2020), 111933, https://doi.org/10.1016/j.rse.2020.111933.
[60] V. Douna, V. Barraza, F. Grings, A. Huete, N. Restrepo-Coupe, J. Beringer, Towards a remote sensing data based evapotranspiration estimation in Northern Australia using a simple random forest approach, J. Arid Environ. 191 (Aug. 2021), 104513, https://doi.org/10.1016/j.jaridenv.2021.104513.
[61] Q. Wang, L. Wang, X. Zhu, Y. Ge, X. Tong, P.M. Atkinson, Remote sensing image gap filling based on spatial-spectral random forests, Sci. Remote Sens. 5 (Jun. 2022), 100048, https://doi.org/10.1016/j.srs.2022.100048.
[62] N.H. Batjes, E. Ribeiro, A. van Oostrum, Standardised soil profile data to support global mapping and modelling (WoSIS snapshot 2019), Earth Syst. Sci. Data 12 (1) (Feb. 2020) 299–320, https://doi.org/10.5194/essd-12-299-2020.
[63] Y. Zhang, B.M. Ayyub, J.F. Fung, Projections of corrosion and deterioration of infrastructure in United States coasts under a changing climate, Resilient Cities Struct 1 (1) (Mar. 2022) 98–109, https://doi.org/10.1016/j.rcns.2022.04.004.
[64] M. Soleimani-Sardo, M. Shirani, V. Strezov, Heavy metal pollution levels and health risk assessment of dust storms in Jazmurian region, Iran, Sci. Rep. 13 (1) (May 2023), https://doi.org/10.1038/s41598-023-34318-1. Art. no. 1.
[65] V. Dentoni, B. Grosso, F. Pinna, A. Lai, O. Bouarour, Emission of fine dust from open storage of industrial materials exposed to wind erosion, Atmosphere 13 (2) (Feb. 2022), https://doi.org/10.3390/atmos13020320. Art. no. 2.
[66] E. Xi, Image classification and recognition based on deep learning and random forest algorithm, Wireless Commun. Mobile Comput. 2022 (Jun. 2022), e2013181, https://doi.org/10.1155/2022/2013181.
[67] A. Ellahyani, M. El Ansari, I. El Jaafari, Traffic sign detection and recognition based on random forests, Appl. Soft Comput. 46 (2016) 805–815.
[68] F. Buendía-Martínez, F. Sutter, J. Wette, L. Valenzuela, A. Fernández-García, Lifetime prediction model of reflector materials for concentrating solar thermal energies in corrosive environments, Sol. Energy Mater. Sol. Cells 224 (Jun. 2021), 110996, https://doi.org/10.1016/j.solmat.2021.110996.
[69] H. Gholami, A. Mohammadifar, D.T. Bui, A.L. Collins, Mapping wind erosion hazard with regression-based machine learning algorithms, Sci. Rep. 10 (1) (Nov. 2020), https://doi.org/10.1038/s41598-020-77567-0. Art. no. 1.
[70] L.-Y. Liu, et al., Natural factors influencing blown sand hazards in beijing, Int. J. Disaster Risk Sci. 2 (Jun) (2011), https://doi.org/10.1007/s13753-011-0008-5.
[71] S. Zamani, M. Mahmoodabadi, N. Yazdanpanah, M.H. Farpoor, Meteorological application of wind speed and direction linked to remote sensing images for the modelling of sand drift potential and dune morphology, Meteorol. Appl. 27 (1) (2020) e1851, https://doi.org/10.1002/met.1851.
[72] M. Mikami, Y. Yamada, M. Ishizuka, T. Ishimaru, W. Gao, F. Zeng, Measurement of saltation process over gobi and sand dunes in the Taklimakan desert, China, with newly developed sand particle counter, J. Geophys. Res. Atmospheres 110 (2005), https://doi.org/10.1029/2004JD004688. D18.
[73] H.C. Hottel, B.B. Woertz, The performance of flat-plate solar-heat collectors, Trans. Am. Soc. Mech. Eng. 64 (2) (Dec. 2022) 91–103, https://doi.org/10.1115/1.4018980.
[74] A.-C. Pescheux, E. Le Baron, O. Raccurt, Characterization of different Moroccan sands to explain their potential negative impacts on CSP solar mirrors, Sol. Energy 194 (Dec. 2019) 959–968, https://doi.org/10.1016/j.solener.2019.11.020.
[75] M.R. Maghami, H. Hizam, C. Gomes, M.A. Radzi, M.I. Rezadad, S. Hajighorbani, Power loss due to soiling on solar panel: a review, Renew. Sustain. Energy Rev. 59 (Jun. 2016) 1307–1316, https://doi.org/10.1016/j.rser.2016.01.044.
[76] S. Ravi, P. D'Odorico, A field-scale analysis of the dependence of wind erosion threshold velocity on air humidity, Geophys. Res. Lett. 32 (2005) 21, https://doi.org/10.1029/2005GL023675.
[77] C. Sansom, P. Comley, P. King, H. Almond, C. Atkinson, E. Endaya, Predicting the effects of sand erosion on collector surfaces in CSP plants, Energy Proc. 69 (May 2015) 198–207, https://doi.org/10.1016/j.egypro.2015.03.023.
[78] G. Xin, N. Huang, J. Zhang, and H. Dun, 'Investigations into the design of sand control fence for Gobi buildings', Aeolian Res, vol. 49, 2021, doi: 10.1016/j.aeolia.2020.100662..
[79] Y. Hao, Y. Xing, L. Li, Erosion-behaviors of the steel structure coating eroded at low erosion-angle in sandstorm environment, Adv. Mater. Res. 383 (390) (Nov. 2011) 3933–3938. https://doi.org/10.4028/www.scientific.net/AMR.383-390.3933.
[80] Y. Hao, L. Li, Z. Zhong, X. He, Research on anti-erosion mechanical properties of steel structure coating, Adv. Mater. Res. 189–193 (Feb. 2011) 1199–1203. https://doi.org/10.4028/www.scientific.net/AMR.189-193.1199.
[81] Y.H. Hao, P.Y. He, A.L. Wu, 'Research on Erosion Mechanical Parameters of Wind-Sand Environmentin the Central and Western Region of Inner Mongolia', *Advanced Materials Research*, vols. 403–408, Trans Tech Publications Ltd, 2012, pp. 1680–1683. https://doi.org/10.4028/www.scientific.net/AMR.403-408.1680.
[82] N. Boddupalli, G. Singh, L. Chandra, B. Bandyopadhyay, Dealing with dust – some challenges and solutions for enabling solar energy in desert regions, Sol. Energy 150 (Jul. 2017) 166–176, https://doi.org/10.1016/j.solener.2017.04.032.
[83] B. Huang, Z. Li, B. Gong, Z. Zhang, B. Shan, O. Pu, Study on the sandstorm load of low-rise buildings via wind tunnel testing, J. Build. Eng. 65 (Apr. 2023), 105821, https://doi.org/10.1016/j.jobe.2022.105821.
[84] S. Boukheir, et al., Physical and chemical reactivity of mechanically primed glass surfaces of CSP reflectors, AIP Conf. Proc. 2303 (1) (Dec. 2020), 150005, https://doi.org/10.1063/5.0028934.

[85] M. Karim, S. Naamane, C. Delord, A. Bennouna, Laboratory simulation of the surface erosion of solar glass mirrors, Sol. Energy 118 (Aug. 2015) 520–532, https://doi.org/10.1016/j.solener.2015.05.044.
[86] K.C. Datsiou, M. Overend, Artificial ageing of glass with sand abrasion, Construct. Build. Mater. 142 (Jul. 2017) 536–551, https://doi.org/10.1016/j.conbuildmat.2017.03.094.
[87] C. Mitsakou, et al., Saharan dust levels in Greece and received inhalation doses, Atmos. Chem. Phys. 8 (Dec. 2008), https://doi.org/10.5194/acpd-8-11967-2008.
[88] N. Bouaouadja, S. Bouzid, M. Hamidouche, C. Bousbaa, M. Madjoubi, Effects of sandblasting on the efficiencies of solar panels, Appl. Energy 65 (1) (Apr. 2000) 99–105, https://doi.org/10.1016/S0306-2619(99)00044-6.
[89] M. Maghami, H. Hizam, C. Gomes, S. Hajighorbani, N. Rezaei, Evaluation of the 2013 southeast asian haze on solar generation performance, PLoS One 10 (8) (Aug. 2015), e0135118, https://doi.org/10.1371/journal.pone.0135118.
[90] H. Pi, B. Sharratt, J. Lei, Windblown sediment transport and loss in a desert–oasis ecotone in the Tarim Basin, Sci. Rep. 7 (1) (Aug. 2017), https://doi.org/10.1038/s41598-017-04971-4. Art. no. 1.
[91] F. Wiesinger, F. Sutter, A. Fernández-García, J. Reinhold, R. Pitz-Paal, 'Sand erosion on solar reflectors: accelerated simulation and comparison with field data', Sol. Energy Mater. Sol. Cells 145 (Feb. 2016) 303–313, https://doi.org/10.1016/j.solmat.2015.10.036.